energies

MDPI

*Article*

# A Hybrid Dynamic Model for the Thermal Compressor Heat Pump and Validation with Experimental Data †

**Ali Salame [1,2], Vincent Lemort [1,*], Pascal Dufour [2] and Madiha Nadri [2]**

[1] Thermodynamics Laboratory, University of Liège (ULiège), Energy Systems Research Unit, 4000 Liège, Belgium; ali.salame@etu.univ-lyon1.fr
[2] Laboratoire d'Automatique et de Génie des Procédés de Paris (LAGEPP), Université Claude Bernard Lyon 1, CNRS UMR 5007, 69100 Villeurbanne, France; pascal.dufour@univ-lyon1.fr (P.D.); madiha.nadir@univ-lyon1.fr (M.N.)
* Correspondence: vincent.lemort@uliege.be; Tel.: +32-4-366-48-01

† This paper is an extended version of our paper published in Salame, A.; Lemort, V.; Dufour, P.; Nadri, M. A Dynamic Model for a Multi-Stage $CO_2$ Thermal Compressor Heat Pump Application. In Proceedings of the ECOS 2025, Paris, France, 29 June–4 July 2025.

**Abstract**

Thermally driven heat pumps primarily use thermal energy to drive a compression cycle. The thermal energy can be waste heat, natural-gas combustion, or solar, helping increase efficiency and reduce greenhouse-gas emissions. We study a thermal compressor heat pump (TCHP) in which Stirling-type thermal compressors (TCs) are heat-driven rather than electrically driven, delivering a nominal heat capacity of 8 kW with $CO_2$ as the refrigerant. Unlike most existing dynamic models of $CO_2$ cycles, which focus on electrically driven or single-stage systems, this work targets a heat-driven multi-stage configuration and includes transient validation. Like any vapor compression cycle (VCC), a TCHP requires a dynamic model for control and optimization; its predictive reliability must be validated on experimental data. We therefore describe the test bench and performance expressions, collect steady-state and transient datasets, and derive a hybrid dynamic model: finite-volume (FV) differential equations for slow components and quasi-static submodels (linear regressions and correlations) for fast elements. The contribution of this work is the development and experimental validation of a hybrid FV model for a multi-stage heat-driven $CO_2$ TCHP. Validation against both steady-state and transient datasets shows good agreement. On 15 steady-state operating points, the model reproduces pressures within ∼1 bar mean absolute error (MAE) and system-level performance (total recovered heat, $COP_{th}$) within ∼6% mean absolute percentage error (MAPE), with $R^2 \gtrsim 0.8$; component heat-rate predictions are within ∼20% MAPE. Under transient step tests on expansion valve openings and burner fan speed, the thermal COP and total recovered heat track within 4% MAPE (up to $R^2 = 0.96$), pressures within 1.5 bar MAE, and the evaporator heat rate within 14–22% MAPE.

**Keywords:** thermal compressor; heat pump; hybrid dynamic model; finite volume; $CO_2$



Academic Editors: Claudia Naldi and Matteo Dongellini

Received: 27 October 2025
Revised: 13 November 2025
Accepted: 18 November 2025
Published: 27 December 2025



## 1. Introduction

In 2023, 80% of the worldwide energy demand was met by burning oil, natural gas, and coal, according to the IEA [1]. Switching entirely to renewables is a long and ongoing process, which we can meet halfway through more efficient usage of the dominant fossil fuels. Despite their great potential, electric heat pumps are still dominated by gas boilers for

reasons beyond the scope of this work. To bridge the gap between gas boilers and electric heat pumps, a Thermal Compressor Heat Pump (TCHP) is proposed, where heat is used to drive the heat pump cycle, benefiting from outdoor conditions. The technology developed by Boostheat uses Stirling-type thermal compressors (TCs) instead of electric compressors. Another environmental advantage is the use of $CO_2$ as a refrigerant. The use of $CO_2$ adds restrictions on cycle configurations due to its high critical pressure (73.8 bar) and low critical temperature (31.1 °C), which also motivates more advanced control strategies to ensure optimal performance. Because control optimization requires a dynamic model, a review of dynamic modeling approaches for vapor compression cycles (VCCs) is given.

The first dynamic models of VCCs date back to the 1980s. Ref. [2] developed a first-order lumped-parameter model for a residential air-to-air heat pump, while ref. [3] presented a finite-volume (FV) model of a heat pump including mass, momentum, and energy balances, whose transient responses were validated against experiments. After three decades of VCC dynamic model development, comprehensive reviews by refs. [4,5] summarized the main dynamic modeling approaches for VCCs, namely the FV, moving-boundary (MB), and data-driven formulations. In practice, these approaches are typically applied to the heat exchangers, while the compressor and expansion valve are represented through algebraic relations: heat exchangers dominate the slow dynamics, whereas the compressor and valve respond more rapidly and can be reasonably approximated by steady-state maps, leading to simplified overall model structures. Much of this literature is ultimately motivated by control design, as physics-based models offer real-time representations of the system and allow investigation of operating ranges that are difficult or unsafe to achieve experimentally.

Among physics-based methods, the most established dynamic formulations are the FV and MB approaches. In general, FV models are built by directly applying conservation equations to discrete control volumes (CVs), resulting in high-order dynamic models that are parametrically rich and capable of representing transient behavior in detail, as demonstrated by [6]. Unlike the MB method, which uses the mean void fraction to represent the two-phase region, the FV approach assumes average fluid properties within each CV, making the prediction of refrigerant charge highly dependent on the discretization level. Ref. [7] applied the FV method to a centrifugal liquid chiller, achieving high accuracy in steady-state predictions and good agreement with transient trends. However, simulations of such models can be computationally demanding due to stiffness arising from the coupling between pressure and mass flow rate. Ref. [8] addressed this issue by assuming a uniform pressure across all CVs so that the pressure variation is computed only once, while the corresponding pressure drops are estimated using quasi-static correlations. More recently, ref. [9] developed a dynamic FV-based model for a VCC adopting the same uniform-pressure approach—referred to as the vanishing-pressure method—and further provided a nonlinear state-space formulation.

The MB approach is often used as a simpler alternative to FV modeling for capturing the transient behavior of VCCs. While FV models gain accuracy from fine spatial discretization [10], MB models aim to capture the essential dynamics of phase-change heat exchangers using lumped parameters and by tracking the moving boundaries between fluid regions (liquid, two-phase, vapor). Ref. [11] provided a technical report detailing the derivation of MB models for evaporators and condensers under various phase-change conditions. A known limitation of the MB approach is that the working fluid phases at component exits must be assumed a priori, which becomes problematic when phase changes occur between single- and two-phase regions or between subcritical and supercritical states. To address this, ref. [12] proposed a switching algorithm to accommodate different component representations depending on the phase. Comparative studies [10,13] have shown

that although FV models are computationally heavier, they are more robust, whereas MB models achieve comparable performance with reduced computational time. Overall, both approaches obey the same physical laws and have proven reliable in reproducing real VCC dynamics.

Several dynamic models have been developed specifically for transcritical $CO_2$ cycles. Ref. [14] implemented a Modelica-based transient model using FV discretization of mass and energy balances, achieving good agreement in both steady-state and transient regimes. Ref. [15] derived a reduced-order model from a detailed 11th-order nonlinear MB model by separating fast and slow dynamics, resulting in a simplified 5th-order version suitable for control design. Ref. [16] proposed an MB model of a transcritical $CO_2$ ejector cycle incorporating variable ejector efficiencies, accurately capturing behavior under changing valve and ejector conditions. Using Simscape, ref. [17] developed an FV dynamic model of a transcritical $CO_2$ heat pump and validated its predictions for mass flow, compressor power, pressures, and COP with good agreement. Ref. [18] presented a one-dimensional distributed FV model for a solar-assisted $CO_2$ water-heating heat pump, demonstrating that lower flow rates lead to higher outlet and compressor temperatures. Ref. [19] developed and validated an FV dynamic model for a reversible $CO_2$ air-to-water heat pump for heating, cooling, and district water applications. Ref. [20] provided a validated Modelica model of a 35 MW transcritical $CO_2$ heat pump for district heating, using segmented heat exchangers and property tables to accurately reproduce plant transients. Most of these implementations were developed in object-oriented environments such as Dymola or Modelica and were generally applied to conventional electric heat pumps with up to two stages.

In contrast, the TCHP model developed in this work is built entirely from scratch in Python 3.10. The targeted application is a thermally driven system with three compression stages and a specifically designed TC. An MB formulation for such a system would depend on the refrigerant regime in the high-pressure heat exchanger (condenser/gas cooler), which must be known or switched a priori. Since the preferred operating range often reaches the supercritical regime, the phase regime cannot be guaranteed in advance. To avoid hybrid MB models requiring regime switching [12], we adopt the FV method. A second motivation for this choice is the inherent robustness of FV models, which is particularly valuable for a multi-stage TCHP with strongly coupled component dynamics. To the authors' best knowledge, this is the first dynamic model of a three-stage heat-pump cycle implemented entirely in Python. The codes are put in the open-source GitHub link found in [21]. The contributions of this work are as follows:

1. Derivation of a hybrid physics–data-based dynamic model for a three-stage $CO_2$ heat pump cycle operating partly in the supercritical regime. Slow components are described with the FV method, while fast ones are quasi-statically tuned from data.
2. Representation of a novel TC—different from conventional electromechanical compressors—using linear regression models identified from a limited set of experimental data.
3. Implementation of the full model from scratch in Python, using an object-oriented structure, and making the code openly available for interested users.

This work is an extension of [22] and it is divided into the following sections. Section 2 described TCHP cycle components and processes, as well as the derived energy expressions from experimental measurements. For the TCHP, Section 3 presents the component submodels, with some parts described by differential equations and others by algebraic relationships. The differential part adopts the FV method, while the quasi-static part is tuned using steady-state data. Finally, Section 4 validates the derived model in both steady-state and transient regimes.

## 2. TCHP Architecture

This section introduces the Boostheat TCHP—a three-stage transcritical $CO_2$ cycle for residential heating—and its experimental setup. We first present the process architecture and operating principle, along with the energy expressions.

### *2.1. System Architecture and Operation*

As illustrated in Figure 1a, the cycle of a TCHP consists of three TCs, three buffers (BUFs), a gas cooler (GC), an evaporator (EV), an internal heat exchanger (IHX), a flash tank (FT), high- and low-pressure expansion valves (HPV and LPV), a one-way valve (OWV), and a fume heat exchanger (FHX). The process occurs on the $CO_2$, water, TCs, and glycol sides as follows:

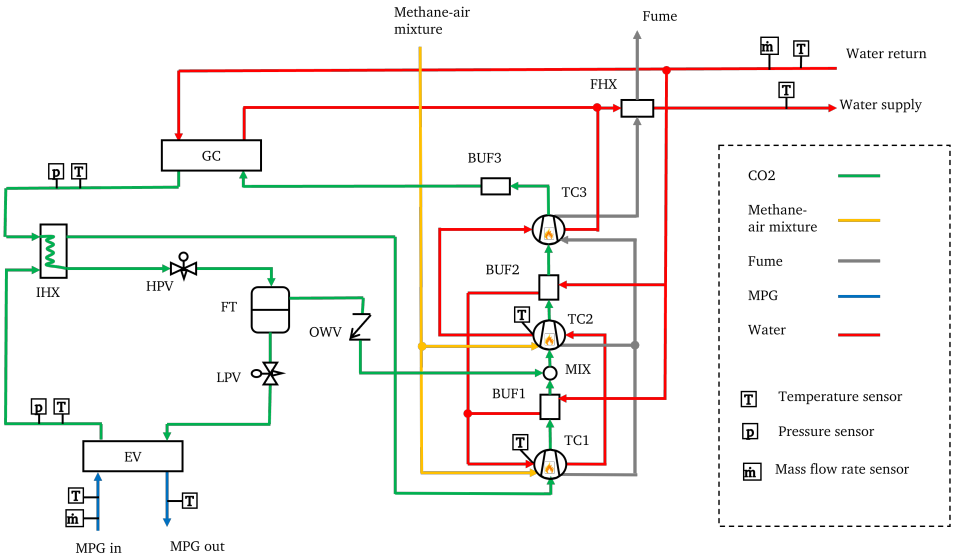


(**a**) Experimental test bench layout.

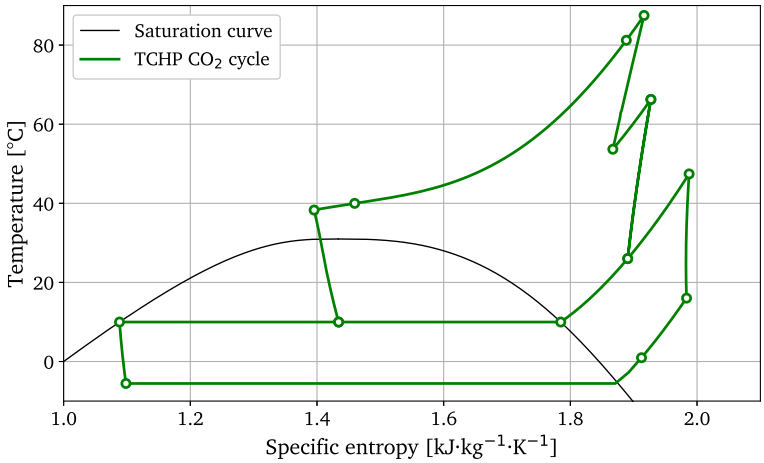


(**b**) Temperature–entropy ($T$-$s$) diagram of $CO_2$ in the cycle.

**Figure 1.** TCHP: (**a**) experimental test bench layout and (**b**) corresponding $T$-$s$ diagram of $CO_2$ in the cycle.

On the $CO_2$ side (green), the state changes are illustrated in the $T$–$s$ diagram shown in Figure 1b: At evaporation pressure, $CO_2$ enters the TC1 and exits at a higher pressure. It is then cooled inside BUF1 by a water flow and mixed with the vapor exiting the FT through an OWV at point MIX before entering the TC2. The $CO_2$ then exits at a higher intermediate

pressure and is cooled again inside BUF2 before entering the TC3. The pressure is then dampened in BUF3, which has no passage for circulating water. In fact, all BUFs after each TC also act as dampers for the pressure waves resulting from compression. At its highest pressure level and temperature, $CO_2$ rejects heat into the water entering the GC. It is then cooled again while passing through one side of the IHX, being cooled by the $CO_2$ exiting the EV from the other side. After exiting the IHX, the $CO_2$ refrigerant is expanded in the HPV and enters the FT. There, the gaseous fraction is re-injected to the suction of the TC2 through an OWV, while the remaining liquid expands in the LPV before entering the EV, where it evaporates and becomes superheated. Finally, additional heat is absorbed in the IHX, completing the cycle and returning the fluid to its initial state.

On the water side (red), heat is recovered from several heat exchangers. A smaller portion of the water flow is directed to the BUFs and the TCs, where it is further subdivided between the first two BUFs and then collected before passing through the TC coolers in sequence from the first to the third stage. The larger portion of the return water goes to the gas cooler, after which the two streams mix again before entering the FHX, where the combustion fumes are cooled. The heated water finally leaves as supply water to the user's end.

On the TCs side: The top parts of the first two TCs (i.e., the heaters) are connected to a burner fan, which delivers a methane/air mixture or burning gas (orange) to the top surfaces of their heaters, where it is ignited to heat the surfaces. The resulting fumes (in gray) from both chambers are collected on the top of TC3 and used to heat its outer heater surface. The fumes are then directed to the FHX, where they are cooled before finally leaving.

On the glycol side (blue): The EV is heated by a glycol mixture of monopropylene glycol and water (MPG). MPG is selected for its low freezing point, allowing the mixture to withstand low outdoor temperatures without solidifying.

### *2.2. Energy Expressions*

In an electrically driven heat pump, the COP is defined as the ratio of the total heat recovery rate to the electric power consumed by the cycle. In this work, heat is the primary source of energy. With a small contribution of electricity compared to heat [23], and for simplicity, a TCHP is evaluated with a thermal COP ($COP_{\mathrm{th}}$), defined as the ratio of the total heat recovery rate ($\dot{Q}_{\mathrm{rec,\,tot}}$) to the fuel thermal power consumed ($\dot{Q}_{\mathrm{fuel}}$),

$$COP_{\mathrm{th}} = \frac{\dot{Q}_{\mathrm{rec,\,tot}}}{\dot{Q}_{\mathrm{fuel}}} \tag{1}$$

The circulating water recovers heat from several heat exchangers (Figure 1a), so the total heat recovery rate is calculated as follows:

$$\dot{Q}_{\mathrm{rec,\,tot}} = \dot{Q}_{\mathrm{gc}} + \dot{Q}_{\mathrm{k1}} + \dot{Q}_{\mathrm{k2}} + \dot{Q}_{\mathrm{k3}} + \dot{Q}_{\mathrm{buf1}} + \dot{Q}_{\mathrm{buf2}} + \dot{Q}_{\mathrm{fhx}} \tag{2}$$

which can also be calculated from the temperature difference between the return and supply water

$$\dot{Q}_{\mathrm{rec,\,tot}} = \dot{m}_{\mathrm{w}} c_{p_{\mathrm{w}}} (T_{\mathrm{w,\,sup}} - T_{\mathrm{w,\,ret}}) \tag{3}$$

while the fuel thermal power is given by

$$\dot{Q}_{\mathrm{fuel}} = \dot{m}_{\mathrm{CH_4}} \cdot \mathrm{LHV}_{\mathrm{CH_4}}, \tag{4}$$

where $\dot{m}_{CH_4}$ is the methane mass flow rate, correlated here as a function of burner fan speed

$$\dot{m}_{CH_4} = \left(\omega_{bf} - 1183\right) 2.49 \times 10^{-8} \tag{5}$$

where the methane lower heating value is $LHV_{CH_4} = 50\ MJ\,kg^{-1}$. An excess-air factor of $EX_{air} = 0.2$ is assumed. The resulting fume mass flow rate (equal to the air–fuel mixture mass flow rate by conservation of mass) is

$$\dot{m}_{fume} = \left[1 + (1 + EX_{air})\, r_s\right] \dot{m}_{CH_4} \tag{6}$$

where $r_s = 17.125$ is the stoichiometric air-to-fuel mass ratio for complete combustion of methane. On the evaporator side, the heat-exchange rate is computed from the temperature difference of the glycol mixture between inlet and outlet,

$$\dot{Q}_{ev} = \dot{m}_{mpg}\, c_{p_{mpg}} \left(T_{mpg,in} - T_{mpg,out}\right) \tag{7}$$

These equations quantify TCHP performance and will be used later to validate the model. In the next section, the hybrid dynamic model of a TCHP is derived.

## 3. TCHP Hybrid Dynamic Model

Each component of a TCHP cycle is first modeled individually and then assembled into a coupled hybrid model consisting of differential equations for the dynamic parts and quasi-static algebraic models for the remaining parts. The final model is referred to as the TCHP hybrid model throughout this work.

In conventional electrically driven heat pump systems, the expansion valve and compressor are often assumed to operate in steady state, as their dynamics are much faster than those of the heat exchangers [11]. Consequently, they are typically represented quasi-statically, while the wall and secondary fluid temperatures in the evaporator and gas cooler (or condenser) are described by differential equations that dominate the system's transient response. This approach reduces complexity and mitigates numerical stiffness.

In a TCHP, however, this assumption no longer holds: the TCs exhibit the slowest dynamics in the cycle, primarily due to the high thermal inertia of their heaters. This inertia causes gradual variations in the working fluid's mass flow rate, temperature, and pressure. Fully representing the TC dynamics would be computationally expensive, so we instead treat the heater temperature (at the outer top surface of the TC)—which evolves slowly—as an input variable (as used in [23]). By selecting heater temperature as the input, the TCs can be modeled using quasi-static models without losing predictive accuracy for the slow dynamics of interest. However, to reach a complete independent TCHP model, the heater-temperature dynamics as a function of burner-fan speed must be modeled separately.

The valves exhibit significantly faster dynamics than the heat exchangers due to their fast response. The fume heat exchanger—being outside the main $CO_2$ cycle—has a faster response due to the direct influence of burner-fan speed.

As a result, the valves, fume heat exchanger, and TCs are modeled quasi-statically, while the dynamic behavior of the cycle heat exchangers, flash tank, and heater temperatures is captured using differential equations.

### *3.1. Differential Equations of the TCHP-HYB Model*

This section is dedicated for the TCHP-HYB model components that are represented with differential equations.

3.1.1. Cycle Heat Exchangers

As shown in Section 2.1, a TCHP cycle incorporates several heat exchangers, including the gas cooler, evaporator, internal heat exchanger, and the first two buffers, all of which are dynamically represented. For modeling the heat exchangers, the following assumptions are made:

- Pressure drops are neglected on both the working-fluid and secondary-fluid sides.
- Heat conduction through the walls is neglected.
- Two-phase regions in the heat exchanger are homogeneous.
- The secondary fluids are assumed to be incompressible.

As illustrated in Figure 2, each heat exchanger is spatially discretized using the FV method into $N$ CVs with a corresponding $i$-axis, where each CV between adjacent solid lines represents uniform pressure $p$ and enthalpy $h$. The mass flow rates $\dot{m}_f$ are considered uniform between adjacent dashed lines, corresponding to the $j$-axis. For the $CO_2$ working fluid, the continuity principle yields the following expression for the time derivative of the density in the $i$-th CV:

$$a_{1i}\frac{\partial p_i}{\partial t} + a_{2i}\frac{\partial h_i}{\partial t} = \dot{m}_{f,j-1} - \dot{m}_{f,j} \tag{8}$$

While applying the energy conservation principle yields the following equation:

$$a_{3i}\frac{\partial p_i}{\partial t} + a_{4i}\frac{\partial h_i}{\partial t} = \dot{m}_{f,j-1}\,h_{j-1} - \dot{m}_{f,j}\,h_j - \dot{Q}_{f,i} \tag{9}$$

where the coefficients are defined as

$$a_{1i} = V_i\left(\frac{\partial \rho_i}{\partial p_i}\right)_{h_i} \qquad a_{2i} = V_i\left(\frac{\partial \rho_i}{\partial h_i}\right)_{p_i} \tag{10}$$

$$a_{3i} = V_i\left[h_i\left(\frac{\partial \rho_i}{\partial p_i}\right)_{h_i} - 1\right] \qquad a_{4i} = V_i\left[h_i\left(\frac{\partial \rho_i}{\partial h_i}\right)_{p_i} + \rho_i\right]. \tag{11}$$

These equations are adopted from [24]. Here, the thermodynamic derivatives $\left(\frac{\partial \rho}{\partial h}\right)_p$ and $\left(\frac{\partial \rho}{\partial p}\right)_h$ denote the partial derivatives of density with respect to enthalpy at constant pressure, and with respect to pressure at constant enthalpy, respectively. As reported by by [8], these equations are stiff and thus result in slow solving. The author therefore proposed considering one mass variation per component so that Equation (8) is applied one time per component and pressure variations are equal across CVs:

$$\frac{\partial p_1}{\partial t} = .... = \frac{\partial p_i}{\partial t} = ... = \frac{\partial p_N}{\partial t} \tag{12}$$

The mass flow is thus uniform across all CVs. The pressure variable is therefore computed once per time step, and pressure drops are not considered, since they are negligible (<1 bar) compared to the operating pressure values of $CO_2$ (30–90 bar). In addition, no mass variation is considered in buffer 1 and the internal heat exchanger, so Equation (8) is not applied to these two components. For heat exchangers with water or glycol mixture as the secondary fluids, the temperature variation is described by

$$\left(mc\frac{\partial T}{\partial t}\right)_{sf,i} = \dot{Q}_{sf,i} + \dot{m}_{sf,j}h_{sf,j} - \dot{m}_{sf,j-1}h_{sf,j-1} \tag{13}$$

In the internal heat exchanger, Equation (9) is applied to both sides as $CO_2$ flows in both. The temperature variation in the heat exchanger wall is modeled as

$$\left(mc\frac{\partial T}{\partial t}\right)_{\text{wall},i} = -(\dot{Q}_{\text{f},i} + \dot{Q}_{\text{sf},i}) \tag{14}$$

The heat transfer rates for the working fluid ($CO_2$) and secondary fluid (water or glycol mixture) are expressed as

$$\dot{Q}_{\text{f},i} = U_{\text{f},i}A_i(T_{\text{wall},i} - T_{\text{f},i}) \tag{15}$$

$$\dot{Q}_{\text{sf},i} = U_{\text{sf},i}A_i(T_{\text{wall},i} - T_{\text{sf},i}) \tag{16}$$

The determination of the heat transfer coefficient ($U_{\text{f}}$) is required to model heat exchange between $CO_2$ and the wall. This coefficient varies with the phase of $CO_2$ (supercritical, subcritical, or two-phase) and the direction of heat transfer (cooling or heating). Although extensive research has been conducted to define suitable correlations for $CO_2$, no universally reliable generalization has emerged. The heat transfer coefficient is calculated from the Nusselt number (Nu) as follows:

$$U = \frac{K \cdot Nu}{d_h} \tag{17}$$

We thus choose from the literature the Nu correlations, based on $CO_2$ phase, as follows:

- For heat exchangers in the supercritical region where pressure is higher than the critical pressure ($p > 73.8$ bar) and $CO_2$ is cooled, the correlation proposed by [25] is used,

$$\text{Nu} = 0.14\,\text{Re}^{0.66}\,\text{Pr}^{0.6} \tag{18}$$

- In the subcritical region where pressure is lower than the critical pressure ($p < 73.8$ bar), in the two-phase regime where vapor quality is between zero and one ($0 < q < 1$): if undergoing evaporation, the heat transfer coefficient is evaluated using the model of [26], while when condensing, the correlation by [27] is used. In both cases, the expressions are complex, so they are not reproduced here.
- In subcritical and single-phase (liquid or vapor) conditions, the standard Dittus–Boelter correlation is applied,

$$\text{Nu} = 0.023\,\text{Re}^{0.8}\,\text{Pr}^{0.4} \tag{19}$$

The standard Dittus–Boelter correlation is also used for the secondary-fluid heat transfer coefficient $U_{\text{sf}}$.

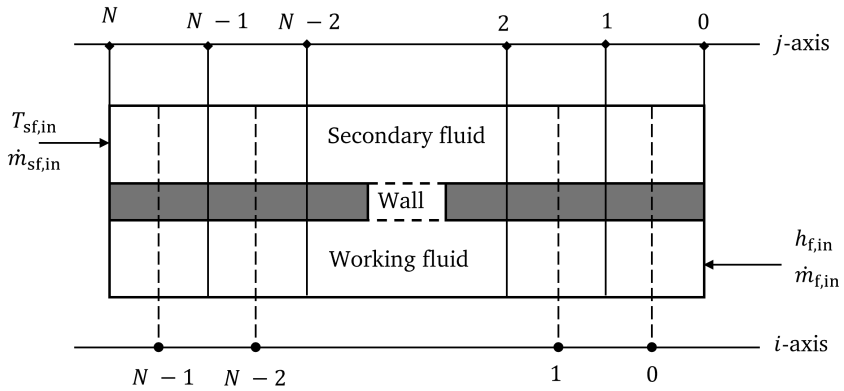


**Figure 2.** Heat exchanger spatial discretization into $N$ CVs. Each CV on the $i$-axis carries uniform pressure and enthalpy, while the $j$-axis carries uniform mass flow rate information.

3.1.2. Flash Tank

For the flash tank, the model provided by [28] is adopted, where it is modeled as a lumped CV with one inlet and two outlets (Figure 3), and the following simplifications are considered:

- Phases are ideally separated.
- The vapor and liquid in the flash tank are at thermodynamic equilibrium.
- The pressure drop within the flash tank is negligible.
- The flash tank is assumed adiabatic.

The governing equations obtained from applying mass and energy balances on the flash tank CV are

$$a_{1\text{ft}}\frac{\partial p_{\text{ft}}}{\partial t} + a_{2\text{ft}}\frac{\partial h_{\text{ft}}}{\partial t} = \dot{m}_{\text{ft,in}} - \dot{m}_{\text{ft,l,out}} - \dot{m}_{\text{ft,v,out}} \tag{20}$$

$$a_{3\text{ft}}\frac{\partial p_{\text{ft}}}{\partial t} + a_{4\text{ft}}\frac{\partial h_{\text{ft}}}{\partial t} = (\dot{m}h)_{\text{ft,in}} - (\dot{m}h)_{\text{ft,l,out}} - (\dot{m}h)_{\text{ft,v,out}} \tag{21}$$

where the coefficients $a_{1\text{ft}}, a_{2\text{ft}}, a_{3\text{ft}}$, and $a_{4\text{ft}}$ are determined by the formulations in (10) and (11). The outlet enthalpies of the vapor and liquid streams are dependent on the state of the refrigerant in the flash tank. If $CO_2$ in the flash tank is in a two-phase state, i.e., the enthalpy of the flash tank $h_{\text{ft}}$ lies between the saturated liquid enthalpy $h_{\text{ft,l}}$ and the saturated vapor enthalpy $h_{\text{ft,v}}$ ($h_{\text{ft,l}} < h_{\text{ft}} < h_{\text{ft,v}}$), the vapor and liquid are assumed to separate perfectly:

$$h_{\text{ft,v,out}} = h_{\text{ft,v}} \tag{22}$$

$$h_{\text{ft,l,out}} = h_{\text{ft,l}} \tag{23}$$

while if $CO_2$ in the flash tank is in a single-phase state, i.e., $h_{\text{ft}} \leq h_{\text{ft,l}}$ or $h_{\text{ft}} \geq h_{\text{ft,v}}$, then the outlet enthalpies of both streams are taken as the mean enthalpy:

$$h_{\text{ft,l,out}} = h_{\text{ft}} \tag{24}$$

$$h_{\text{ft,v,out}} = h_{\text{ft}} \tag{25}$$

The mass flow rates of the streams into and out of the flash tank are discussed later in Section 3.2.2.

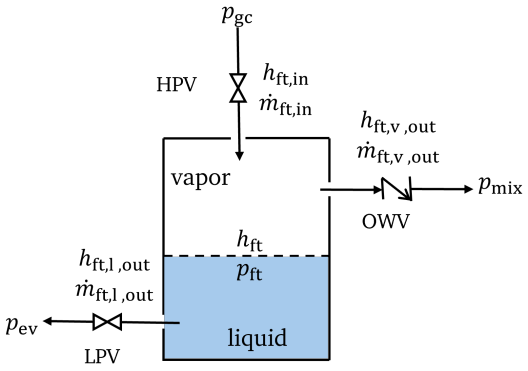


**Figure 3.** Flash tank schematic with the corresponding flow streams.

3.1.3. TC Heaters

This section models the dynamic variation in the heaters' temperatures. The heaters are externally heated by methane–air combustion and internally cooled by $CO_2$. A detailed model of the combustion chamber and the TC internals is not developed here because their internal thermal and fluid processes evolve much faster (on the order of milliseconds to seconds) than the overall TCHP cycle dynamics (tens of seconds to minutes). In

other words, their states reach steady conditions almost instantly compared to the slower system variables.

Therefore, the TC is treated as a black box whose net effect on the heaters is captured through measurable control inputs: the burner-fan speed ($\omega_{bf}$), representing external heat input, and the TC rotational speed ($\omega_m$), representing internal cooling. This simplification allows the model to focus on the dominant, slower thermal dynamics of the TCHP without resolving the fast combustion and compression transients that have negligible impact at the system time scale.

System identification is then performed using experimental step tests (transient data) to obtain suitable models. Three different data sets are used: (i) a pseudo-random binary sequence (PRBS) applied to the burner fan speed, (ii) step tests, and (iii) step tests on the motor rotational speeds. The PRBS excitation ensures coverage of the minimum and maximum burner fan speeds. The input ranges for motor rotational speeds are $60 \leq \omega_{m1}, \omega_{m2} \leq 240$ rpm, and for burner fan speed, it is $2000 \leq \omega_{bf} \leq 9500$ rpm. The dynamics of the heater temperatures $T_{h1}$ and $T_{h2}$ are represented by nonlinear system identification models. The parameters of these models are obtained through minimization of the ordinary least squares error between the measured and predicted $T_{h1}$ and $T_{h2}$, respectively, leading to the following identified discrete-time models:

$$T_{h1}(k+1) = 0.45 + T_{h1}(k) + 2 \times 10^{-4}\,\omega_{bf}(k) - 7.6 \times 10^{-9}\,\omega_{bf}^2(k) - 1.1 \times 10^{-3}\,\omega_{m1}(k) \quad (26)$$

$$T_{h2}(k+1) = 0.51 + T_{h2}(k) + 1.8 \times 10^{-4}\,\omega_{bf}(k) - 6.4 \times 10^{-9}\,\omega_{bf}^2(k) - 1.3 \times 10^{-3}\,\omega_{m2}(k) \quad (27)$$

The fitting of both models is shown in Figures 4 and 5, which indicate relatively high accuracy, with MAEs of 15.9 K and 16.8 K and $R^2$ scores of 0.96 and 0.94 for heater temperatures 1 and 2, respectively. Relative to the heater temperature range of 220 to 800 °C (about 580 K difference), the MAE values correspond to relative errors below 3%. This demonstrates that the identified models reliably predict heater temperature variations and can be confidently used as part of the TCHP-HYB model. The figures also reveal that burner fan speed has a stronger influence on heater temperature compared to rotational speed and thus a greater impact on system operation.

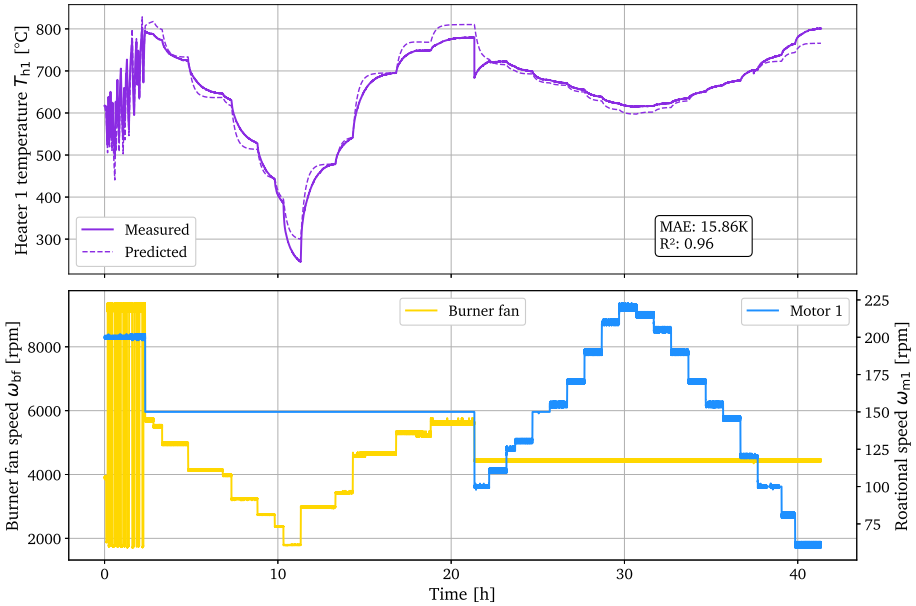


**Figure 4.** Heater 1 temperature $T_{h1}$ identified model validation. MAE is 15.86 K and $R^2$ is 0.96, indicating a good fit. The bottom plot shows the burner fan speed and motor 1 rotational speed over time, illustrating their influence on $T_{h1}$ dynamics.

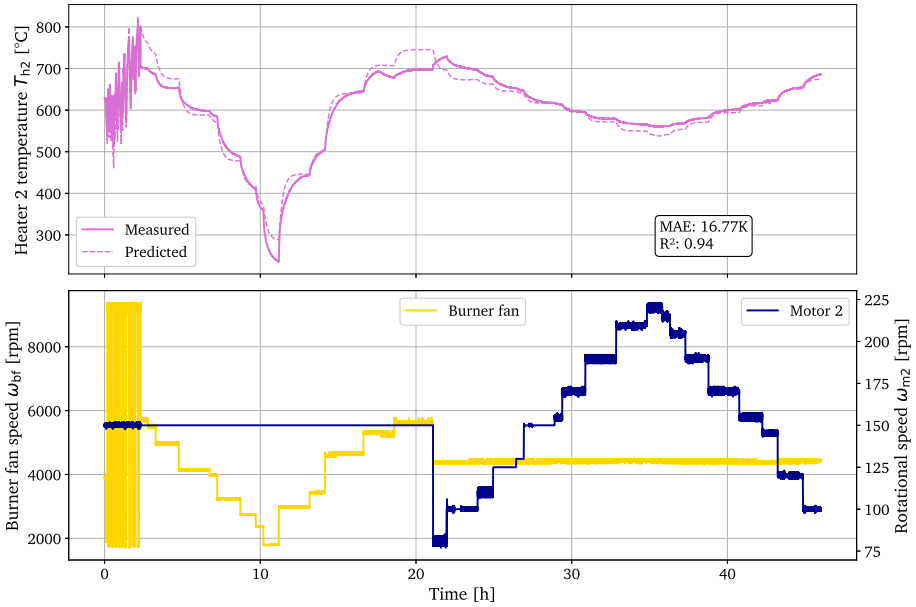


**Figure 5.** Heater 2 temperature $T_{h2}$ identified model validation. MAE is 16.77 K and $R^2$ is 0.94, indicating a good fit. The bottom plot shows the burner fan speed and motor 2 rotational speed over time, illustrating their influence on $T_{h2}$ dynamics.

### *3.2. Static Part of the TCHP-HYB Model*

This section is dedicated to the part of the TCHP-HYB model represented quasi-statically. Unlike the differential equations, which are mostly deterministic—except for the heater temperatures described—these models rely greatly on tuning using real data. For this purpose, the steady-state TCHP dataset is used to tune the quasi-static models.

#### 3.2.1. Thermal Compressors

The TCs are crucial components in the TCHP cycle due to their contribution to the mass flow rates, discharge temperatures, and heat recovery rate through their coolers. Due to the small number of samples, and to avoid overfitting, a simple linear regression (LR) model is chosen. More about used data can be found in [23]. The evaporator outlet mass flow rate ($\dot{m}_{tc1}$), discharge temperature ($T_{tc1,\,dis}$), and heat recovery ($\dot{Q}_{k1}$) are as follows:

$$\dot{m}_{tc1} = 10^{-3}\left(-51.7\,r_{p1} + 0.025\,T_{h1} + 0.024\,T_{tc1,w,in} + 0.17\,\omega_{m1} + 0.086\,T_{tc1,suc}\right) + 0.026 \quad (28)$$

$$T_{tc1,dis} = -28.2\,r_{p1} + 0.031\,T_{h1} + 3.1\,T_{tc1,w,in} + 0.1\,\omega_{m1} - 1.0\,T_{tc1,suc} + 266.5 \quad (29)$$

$$\dot{Q}_{k1} = \quad 827\,r_{p1} + 0.23\,T_{h1} + 36\,T_{tc1,w,in} + 3.9\,\omega_{m1} - 8.6\,T_{tc1,suc} - 1900 \quad (30)$$

The TC2 induced mass flow rate ($\dot{m}_{tc2}$), discharge temperature ($T_{tc2,\,dis}$), and heat recovery ($\dot{Q}_{k2}$) are as follows:

$$\dot{m}_{tc2} = 10^{-3}\left(-84.7\,r_{p2} + 0.038\,T_{h2} + 0.46\,T_{tc2,w,in} + 0.084\,\omega_{m2} - 0.27\,T_{tc2,suc}\right) + 0.092 \quad (31)$$

$$T_{tc2,dis} = 19.8\,r_{p2} + 9.5 \times 10^{-3}\,T_{h2} + 1.27\,T_{tc2,w,in} + 0.04\,\omega_{m2} + 0.57\,T_{tc2,suc} + 246.55 \quad (32)$$

$$\dot{Q}_{k2} = \quad 1914\,r_{p2} + 0.36\,T_{h2} - 5.7\,T_{tc2,w,in} + 3.25\,\omega_{m2} + 18.4\,T_{tc2,suc} - 2700 \quad (33)$$

LR models for TC3 define the gas cooler inlet mass flow rate ($\dot{m}_{tc3}$), so the third buffer between TC3 and the gas cooler is considered part of this model; the discharge temperature ($T_{tc3,\,dis}$), and heat recovery ($\dot{Q}_{k3}$) are as follows:

$$\dot{m}_{tc3} = 10^{-4}\left(-769\,r_{p3} + 0.58\,T_{h2} - 4.3\,T_{tc3,w,in} + 0.081\,\omega_{m3} + 2.5\,T_{tc3,suc}\right) + 0.056 \quad (34)$$

$$T_{tc3,dis} = -58.9\,r_{p3} + 0.059\,T_{h2} + 1.2\,T_{tc3,w,in} - 0.01\,\omega_{m3} + 0.36\,T_{tc3,suc} + 298 \quad (35)$$

$$\dot{Q}_{k3} = 203.2\,r_{p3} + 1.13\,T_{h2} - 5.6\,T_{tc3,w,in} + 3.5\,\omega_{m3} + 6.3\,T_{tc3,suc} - 990 \quad (36)$$

The independent variables are pressure ratio $r_{p3}$, second heater temperature $T_{h2}$ to include inertia (since no direct measurements of heater temperature on TC3 are provided), inlet water temperature $T_{tc3,w,in}$ which leaves TC2 cooler, rotational speed $\omega_{m3}$, and suction temperature $T_{tc3,suc}$. The fitting of the LR model on TC1, TC2, and TC3 outputs is illustrated using parity plots in Figures 6–8. The accuracies (MAE, MAPE, and $R^2$) are summarized in Table 1. The resulting metrics indicate that the models achieve acceptable accuracy levels. Having accurate TC models is important for predicting mass flow rates, discharge temperatures, and cooler heat transfer rates during simulation, as they contribute to the overall prediction accuracy of the TCHP-HYB model.

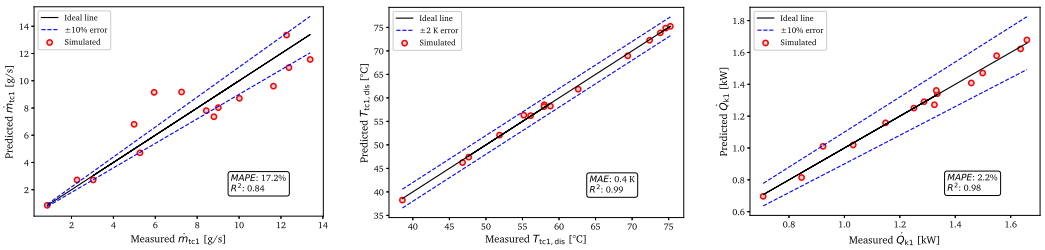


(**a**) Mass flow rate. (**b**) Discharge temperature. (**c**) Cooler heat transfer rate.

**Figure 6.** LR model steady-state parity plots showing the predicted outputs of TC1 compared to measured ones.

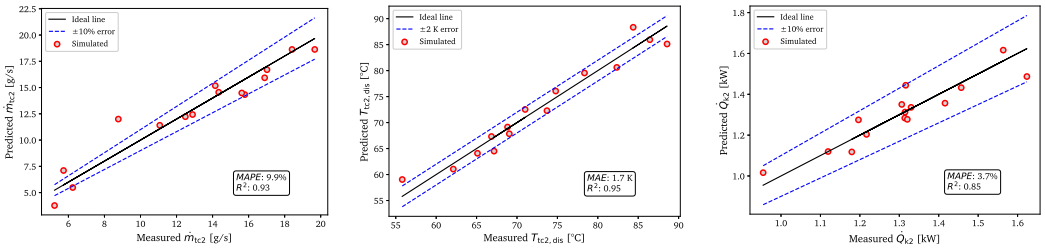


(**a**) Mass flow rate. (**b**) Discharge temperature. (**c**) Cooler heat transfer rate.

**Figure 7.** LR model steady-state parity plots showing the predicted outputs of TC2 compared to measured ones.

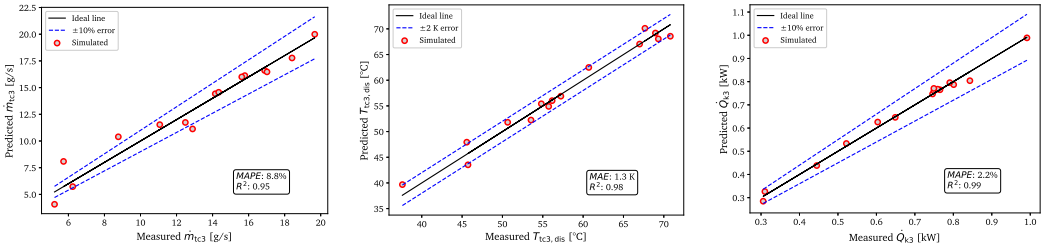


(**a**) Mass flow rate. (**b**) Discharge temperature. (**c**) Cooler heat transfer rate.

**Figure 8.** LR model steady-state parity plots showing the predicted outputs of TC3 compared to measured ones.

**Table 1.** TC models prediction accuracy for each output: MAPE for flow and power variables, MAE for temperatures, and $R^2$ for all outputs.

| Output Variable | MAPE [%]/MAE [K] | $R^2$ |
|---|---|---|
| $\dot{m}_{tc1}$ | 17.2% | 0.84 |
| $T_{tc1,\,dis}$ | 0.4 K | 0.99 |
| $\dot{Q}_{k1}$ | 2.2% | 0.98 |
| $\dot{m}_{tc2}$ | 9.9% | 0.93 |
| $T_{tc2,\,dis}$ | 1.7 K | 0.95 |
| $\dot{Q}_{k2}$ | 3.7% | 0.85 |
| $\dot{m}_{tc3}$ | 8.8% | 0.95 |
| $T_{tc3,\,dis}$ | 1.3 K | 0.98 |
| $\dot{Q}_{k3}$ | 2.2% | 0.99 |

#### 3.2.2. Valves

In a TCHP cycle, there are three flow streams connecting the flash tank with different cycle components (Figure 3). The outlet liquid mass flow rate $\dot{m}_{ft,l,out}$ flows through a low-pressure expansion valve, connecting the flash tank to the inlet of the evaporator. The inlet mass flow rate $\dot{m}_{ft,in}$ flows through a high-pressure valve. Both these valves are the electronic type, and their openings can be regulated. On the other hand, the outlet vapor mass flow rate $\dot{m}_{ft,v,out}$ flows through a one-way valve of fixed opening area to the suction point of the second TC (MIX point). The flow through these valves is considered isenthalpic and is modeled using the following equations:

$$\dot{m}_{lpv} = (C_d A)_{lpv} \sqrt{\rho_{ft,l}(p_{ft} - p_{ev})} \tag{37}$$

$$\dot{m}_{hpv} = (C_d A)_{hpv} \sqrt{\rho_{gc}(p_{gc} - p_{ft})} \tag{38}$$

$$\dot{m}_{owv} = (C_d A)_{owv} \sqrt{\rho_{ft,v}(p_{ft} - p_{mix})} \tag{39}$$

The combined value of the product $(C_d A)$ of the low- and high-pressure valves can be obtained by a regression relation with the percentage valve opening $\varphi$ [28]:

$$(C_d A)_{lpv} = 10^{-9}\left(-100 + 6\,\varphi_{lpv}\right) \tag{40}$$

$$(C_d A)_{hpv} = 10^{-9}\left(63.8 + 4.76\,\varphi_{hpv}\right) \tag{41}$$

The coefficients are obtained by tuning against TCHP steady-state data, where the mass flow rate in the low-pressure valve is equal to that in TC1 and in the high-pressure valve equal to that in TC2 and TC3 considering steady-state conditions. The resulting predicted mass flow rates in the low- and high-pressure valves from the fitted correlations are represented in Figure 9.

The effective flow area of the one-way valve is assumed constant and set to

$$(C_d A)_{owv} = 10^{-6} \tag{42}$$

Due to missing pressure measurements at the mixing point in the TCHP steady-state data, the correlation could not be calibrated with real data. The chosen value was instead selected arbitrarily based on simulations of the complete TCHP-HYB model. The importance of determining flow rates through the valves lies in well establishing pressure and enthalpy variations inside the flash tank as well as the connected components (evaporator, gas cooler, and mixing point at TC2 suction), and thus affecting the overall predictions of the TCHP-HYB model.

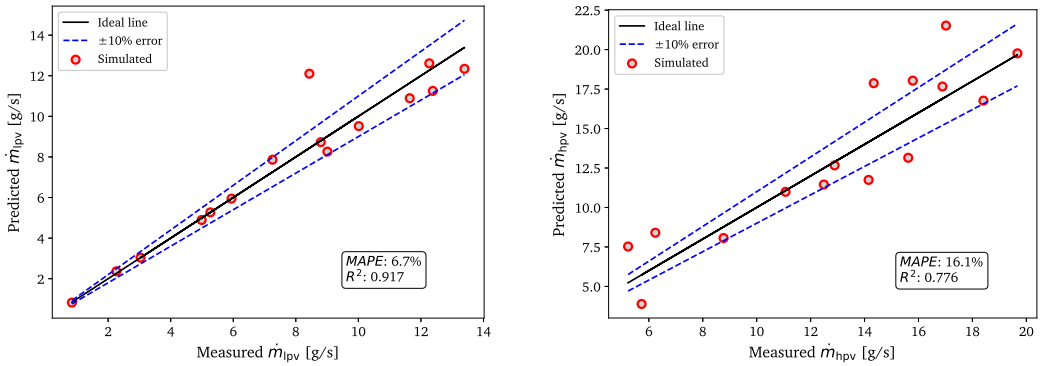


(**a**) Low pressure valve. (**b**) High pressure valve.

**Figure 9.** Expansion valve models steady-state parity plots showing the predicted mass flow rates from fitted Equations (40) and (41), compared to the measured ones.

#### 3.2.3. Fume Heat Exchanger

In a TCHP cycle, the fume heat exchanger is the last heat exchanger where water recovers heat. Its heat exchange rate is considered faster than cycle heat exchangers from Section 3.1.1, as it is directly influenced by the burner fan speed instead of the heater temperatures. For this reason, it is modeled quasi-statically using the logarithmic mean temperature difference (LMTD) method. Figure 10 shows the schematic of the fume heat exchanger, where the inlet fume temperature $T_{\text{fhx,fume,in}}$ rejects heat to the inlet water temperature $T_{\text{fhx,w,in}}$, and the streams leave at $T_{\text{fhx,fume,out}}$ and $T_{\text{fhx,w,out}}$, respectively. Along with the mass flow rates $\dot{m}_{\text{w}}$ and $\dot{m}_{\text{fume}}$. According to the LMTD method,

$$\dot{Q}_{\text{fhx}} = (AU)_{\text{fhx}}\, \Delta T_{\text{lm}} \tag{43}$$

where:

$$\Delta T_{\text{lm}} = \frac{\Delta T_1 - \Delta T_2}{\ln(\Delta T_1 / \Delta T_2)} \tag{44}$$

with:

$$\Delta T_1 = T_{\text{fhx,fume,in}} - T_{\text{fhx,w,out}} \qquad \Delta T_2 = T_{\text{fhx,fume,out}} - T_{\text{fhx,w,in}} \tag{45}$$

From the inlet and outlet temperatures, mass flow rate on both sides, and the measured heat transfer rate at the fume heat exchanger, $(AU)_{\text{fhx}}$ can be retrieved from data and then tuned as a function of $\omega_{\text{bf}}$ and $T_{\text{fhx,w,in}}$:

$$(AU)_{\text{fhx}} = -32.7\dot{m}_{\text{w}} + 0.0035\,\omega_{\text{bf}} + 1.9 \tag{46}$$

Substituting this fitted correlation in Equation (43) gives a MAPE of 15.8% and an $R^2$ of 0.96 between predicted and measured heat exchange rate (Figure 11).

For integrating in the TCHP-HYB model, an LMTD iterative model is proposed (Figure 12). At each iteration it finds the appropriate $T_{\text{fhx,w,out}}$, $T_{\text{fhx,fume,out}}$, and $\dot{Q}_{\text{fhx}}$ by taking $T_{\text{fhx,fume,in}}$, $T_{\text{fhx,w,in}}$, $\dot{m}_{\text{w}}$, $\dot{m}_{\text{fume}}$, fume and water specific heats ($c_{p_{\text{fume}}}$ and $c_{p_{\text{w}}}$), and tuned $(AU)_{\text{fhx}}$ as inputs. In short, the method computes these variables while ensuring the energy balance on both water and fume sides is satisfied. The iteration continues until the difference between guessed and computed $\dot{Q}_{\text{fhx}}$ is less than $10^{-6}$. The inlet fume temperature is correlated from steady-state data as a function of burner fan speed,

$$T_{\text{fhx,fume,in}} = 0.056\,\omega_{\text{bf}} - 36.5 \tag{47}$$

while the inlet water temperature is computed from other heat exchangers in the TCHP.

After deriving all these component-level models, they are connected to form a final system-level complete TCHP to be validated.

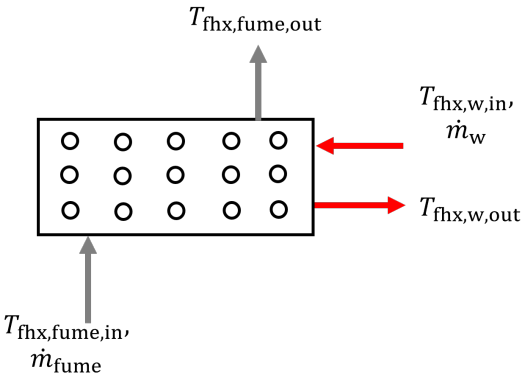


**Figure 10.** Fume heat exchanger schematic.

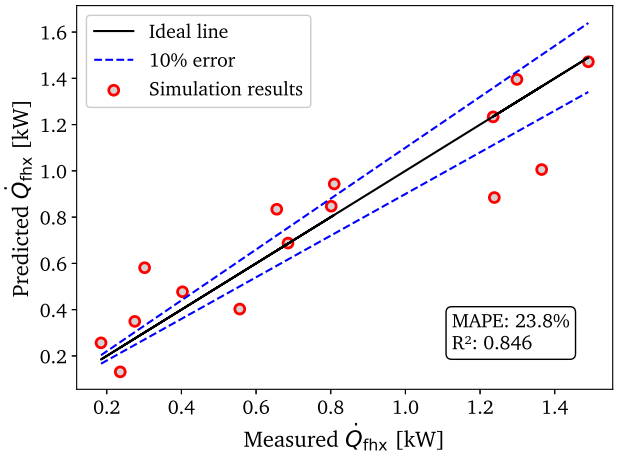


**Figure 11.** Fume heat exchanger model steady-state parity plots showing the predicted heat transfer rate from fitted Equation (46) compared to the measured ones.

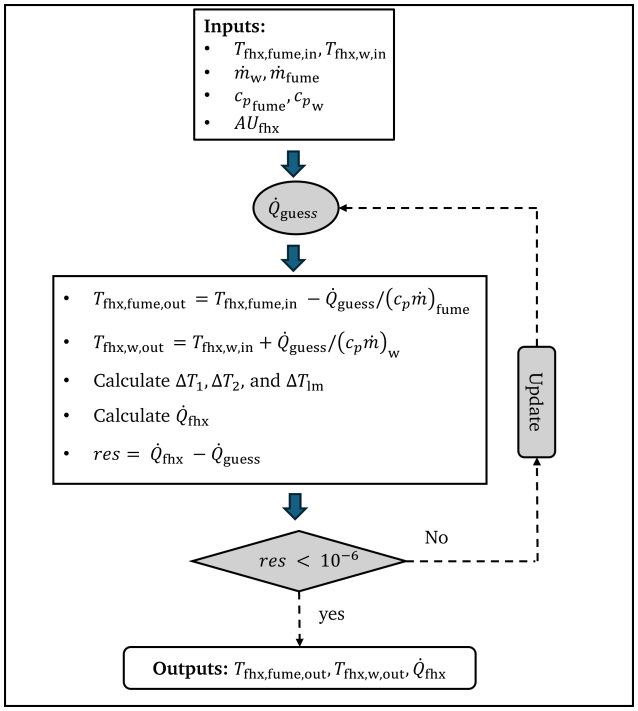


**Figure 12.** Fume heat exchanger LMTD iterative method.

## 4. Model Validation

The validation of the TCHP-HYB model is conducted on the TCHP steady-state data and the open-loop transient data described in Section 2. The steady-state data consist of 15 experimental samples at steady state under various operating conditions, while the transient data contain the step tests on the inputs.

### *4.1. Steady State*

The validation is carried out on the measured outputs, which are high pressure $p_{gc}$, low pressure $p_{ev}$, supply water temperature $T_{w,sup}$, glycol mixture outlet temperature $T_{mpg,out}$, the evaporator heat transfer rate $\dot{Q}_{ev}$, the total recovered heat transfer rate $\dot{Q}_{rec,tot}$, and the thermal COP $COP_{th}$ (calculations in Section 2.2). These outputs were selected as performance indicators relevant for later control development. To assess the accuracy of the model's steady-state predictions, parity plots comparing predicted and measured values are presented.

Figure 13 shows parity plots for high pressure and the gas cooler heat transfer rate. Simulation results for both outputs are in good agreement with the data. High pressure and gas cooler heat transfer rate are predicted with average MAPE values of 1.7% and 17.5%, respectively. This accuracy depends on other predictions such as inlet temperature (Figure 8b), entering mass flow rate (Figure 8a), leaving mass flow rate (Figure 9b), as well as the empirical heat transfer coefficient correlations in single-phase cooling, subcritical condensation, and supercritical cooling discussed in Section 3.1.1. Overall, the prediction accuracy is considered acceptable.

Figure 14 shows parity plots for low pressure and the evaporator heat transfer rate. Simulation results for both outputs also align well with the data. Low pressure and evaporator heat transfer rate are predicted with average MAPE values of 3.2% and 19.9%, respectively. This accuracy depends on other predictions such as inlet temperature (Figure 6b), entering mass flow rate (Figure 9a), leaving mass flow rate (Figure 6a), as well as the empirical heat transfer coefficient correlations in subcritical evaporation and single-phase heating (Section 3.1.1). Thus, the predictions are judged acceptable.

Figure 15 presents parity plots for the total recovered heat transfer rate and the thermal COP. Simulation results for both outputs are in good agreement with the data. These predictions are directly influenced by the accuracy of the gas cooler heat transfer rate (Figure 13); the accuracies at the coolers (Figures 6c, 7c and 8c), the buffers, and the fume heat exchanger (Figure 11) are also relevant. This explains why the error on the total recovered heat transfer is smaller than that on the gas cooler.

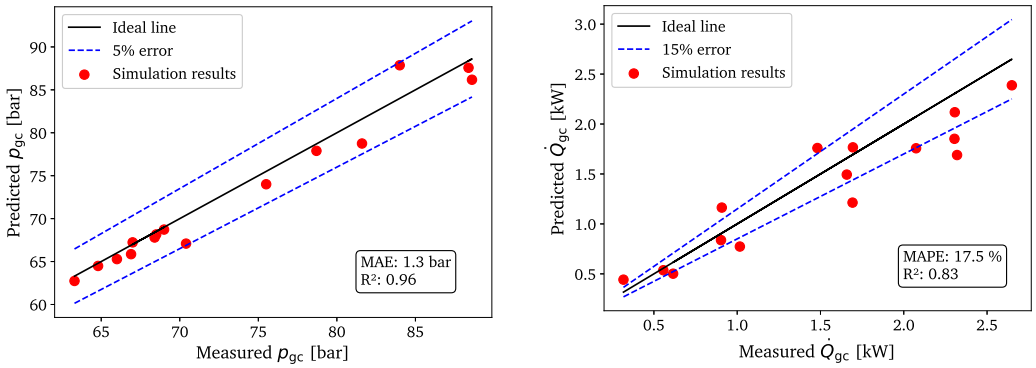


(**a**) High pressure. (**b**) Gas cooler heat transfer rate.

**Figure 13.** TCHP-HYB model steady-state parity plots showing the gas cooler predicted outputs compared to the measured ones.

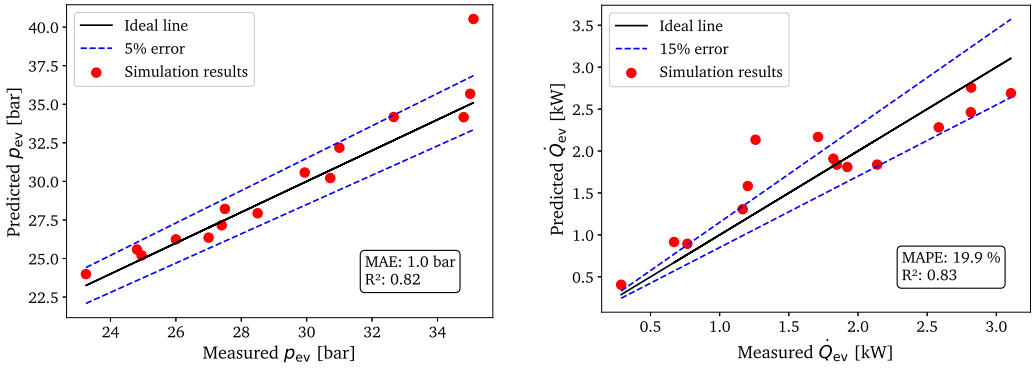


(**a**) Low pressure. (**b**) Evaporator heat transfer rate.

**Figure 14.** TCHP-HYB model steady-state parity plots showing the evaporator predicted outputs compared to the measured ones.

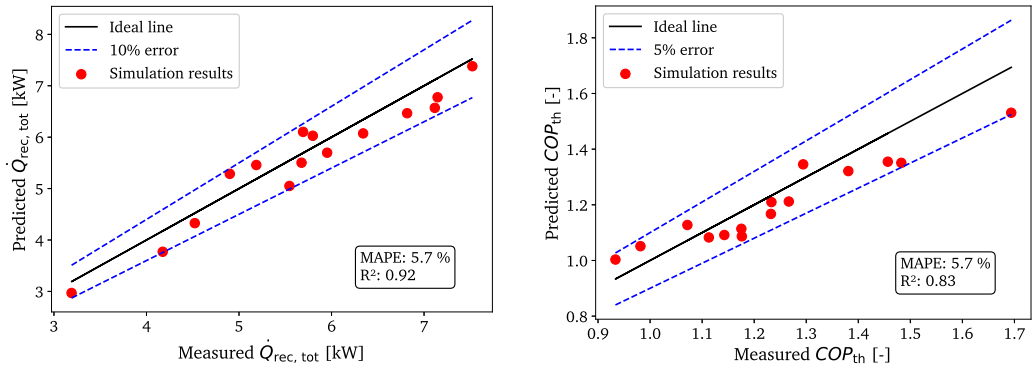


(**a**) Total heat recovery rate. (**b**) Thermal COP.

**Figure 15.** TCHP-HYB model steady-state parity plots showing the overall performance outputs of the TCHP.

The importance of showing $R^2$ is to evaluate whether the model changes are coherent with the data under different operating conditions, where the inputs are distinct in each case. The resulting MAPE and $R^2$ for the main model predictions in steady state are summarized in Table 2. The model shows strong explanatory power across most variables, with high $R^2$ values (>0.8). Overall, the model performs well in fitting and predicting key variables, although there are accuracy limitations in the heat-exchange rates for the evaporator and gas cooler that are justified by influencing other predicted inputs and the multi-stage error accumulation.

**Table 2.** MAPE, MAE (for pressure), and $R^2$ of model output predictions under steady-sate data conditions.

| Output | MAPE [%] or MAE [bar] | $R^2$ |
|---|---|---|
| $p_{gc}$ | 1.3 | 0.96 |
| $p_{ev}$ | 1 | 0.82 |
| $\dot{Q}_{ev}$ | 19.9% | 0.83 |
| $\dot{Q}_{gc}$ | 17.5% | 0.83 |
| $\dot{Q}_{rec,tot}$ | 5.7% | 0.92 |
| $COP_{th}$ | 5.7% | 0.83 |

### *4.2. Transient Validation*

The transient validation focuses on varying three key inputs: the low-pressure valve opening $\varphi_{\mathrm{lpv}}$, the high-pressure valve opening $\varphi_{\mathrm{hpv}}$, and the burner-fan speed $\omega_{\mathrm{bf}}$, which in turn governs the heater temperatures. The variation is performed in step-test fashion. These tests are used here to validate the model's ability to reproduce transient changes in the validated outputs, except for the gas cooler heat transfer rate, which is not available from the transient test data.

Figure 16 illustrates the outputs when the low-pressure valve opening is varied in a step-test manner (LPV test). The greatest influence is seen on the low-pressure level, owing to its strong correlation with mass-flow-rate changes driven by the low-pressure valve. It also affects the evaporator heat transfer rate. Both transient trends are well captured by the model. A smaller impact is observed on high pressure and on the total recovered heat transfer rate. However, a discrepancy is observed in how these outputs are influenced. Specifically, variations in high pressure are mirrored in the total recovered heat and consequently in the thermal COP. This reflects the strong coupling between high-pressure dynamics and overall heat recovery. In contrast, the influence of changes in the low-pressure valve opening is not fully propagated to the high-pressure side, indicating a limitation in the current model's ability to capture this interaction.

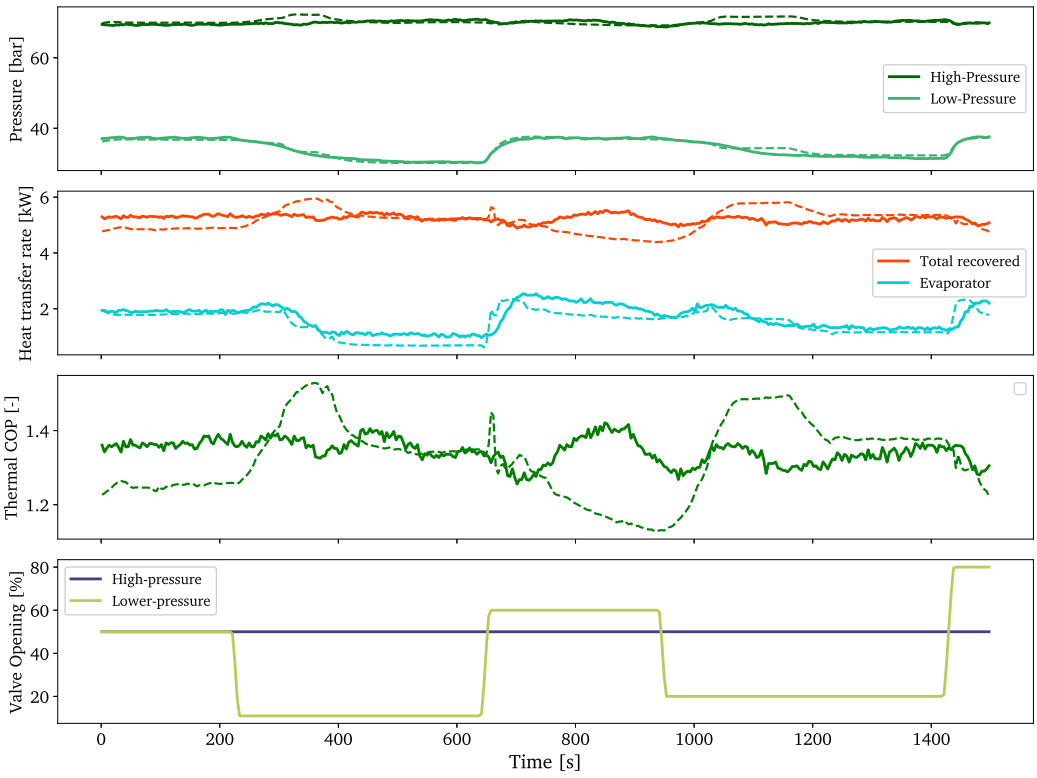


**Figure 16.** TCHP-HYB model transient validation with real experimental data varying the low-pressure valve opening. The real data is in solid, while simulated model is dashed.

Figure 17 presents the output variations when the high-pressure valve opening is changed in a step-test manner (HPV test). The largest influence is observed on the high-pressure level, where the model exhibits transient behavior consistent with the data. The effect on the total heat recovery rate due to changes in high pressure is also evident and well captured. Closing the valve and increasing the outlet mass flow rate causes the pressure to rise to the supercritical state; however, the total recovered heat and the thermal COP decrease. This is due to a large reduction in mass flow rate, such that the heat transfer

becomes less efficient. Some lag is also observed between the predicted and measured outputs, which is attributed to the single mass or pressure variation being governed by quasi-static mass flow rate equations.

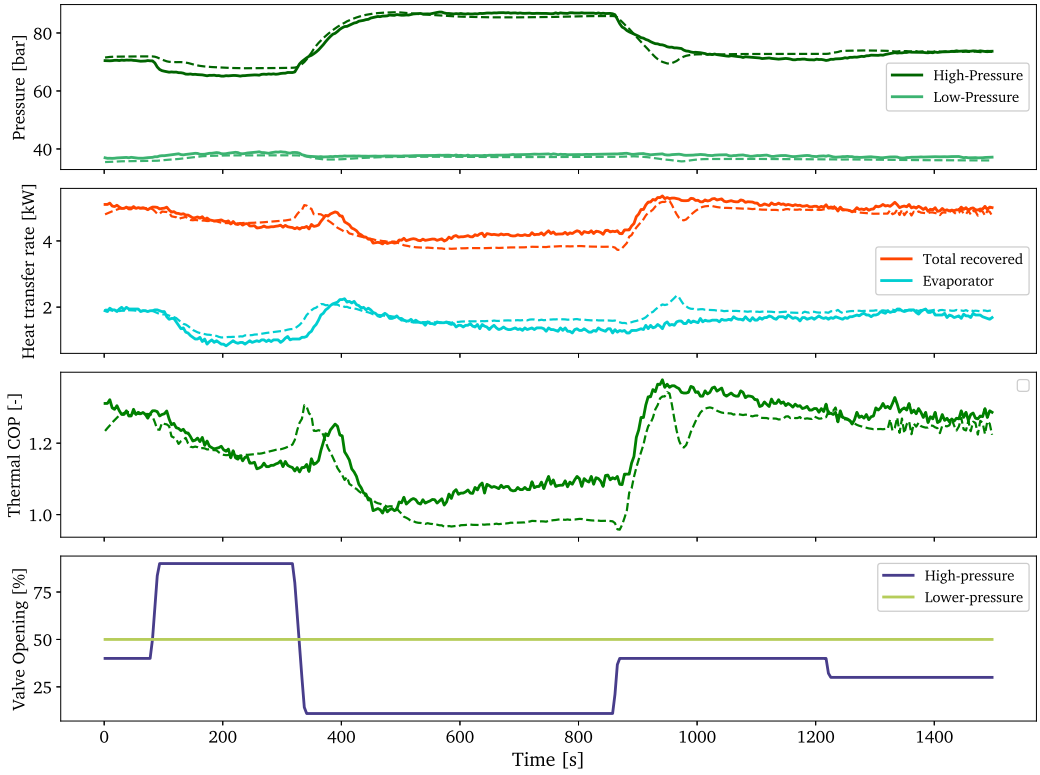


**Figure 17.** TCHP-HYB model transient validation with real experimental data varying the high-pressure valve opening. The real data is in solid, while simulated model is dashed.

Figure 18 shows several step changes applied to burner fan speed over a period of 250 min, reflecting the slow dynamics of the heater temperatures (BF test). Variations in burner fan speed (together with heater 1 and heater 2 temperatures) directly affect the mass flow rates, discharge temperatures, and the cooler heat-transfer rates of the TCs, which explains the observed variations in all outputs. The fast response due to the sudden change in the step test is not shown either with data or with the model. This can be due to small step changes that are not too relevant to total recovered heat. So we evaluate our model with the PRBS performed on the burner fan speed.

The model successfully captures both the fast response caused by sudden changes in BF and the slower response driven by the gradual evolution of heater temperatures.

The resulting MAPE and $R^2$ metrics for each test are summarized in Table 3. Negative $R^2$ values in the LPV and HPV tests for gas cooler and evaporator pressures, respectively, stem from weak input–output correlations and measurement noise, which limit the model's explanatory power in those cases. In particular, the limited influence of the LPV on the high-pressure side, noted earlier, is reflected here in poor prediction of $p_{gc}$. In contrast, the BF tests (BF in Table 3) show an acceptable fit across all outputs due to the direct influence of BF on heater temperatures and thus on overall system behavior.

From the $R^2$ results, we conclude that HPV and BF have the strongest impact on system performance and are therefore critical control variables whose regulation can optimize key outputs. The negative $R^2$ values in the LPV and HPV cases for gas cooler and evaporator outputs may also reflect unmeasured dynamics in intermediate components (i.e., the flash tank and first buffer), for which no instrumentation is available. Nevertheless, the

model effectively reproduces the dominant dynamics associated with HPV and BF and is considered suitable for subsequent control and optimization studies.

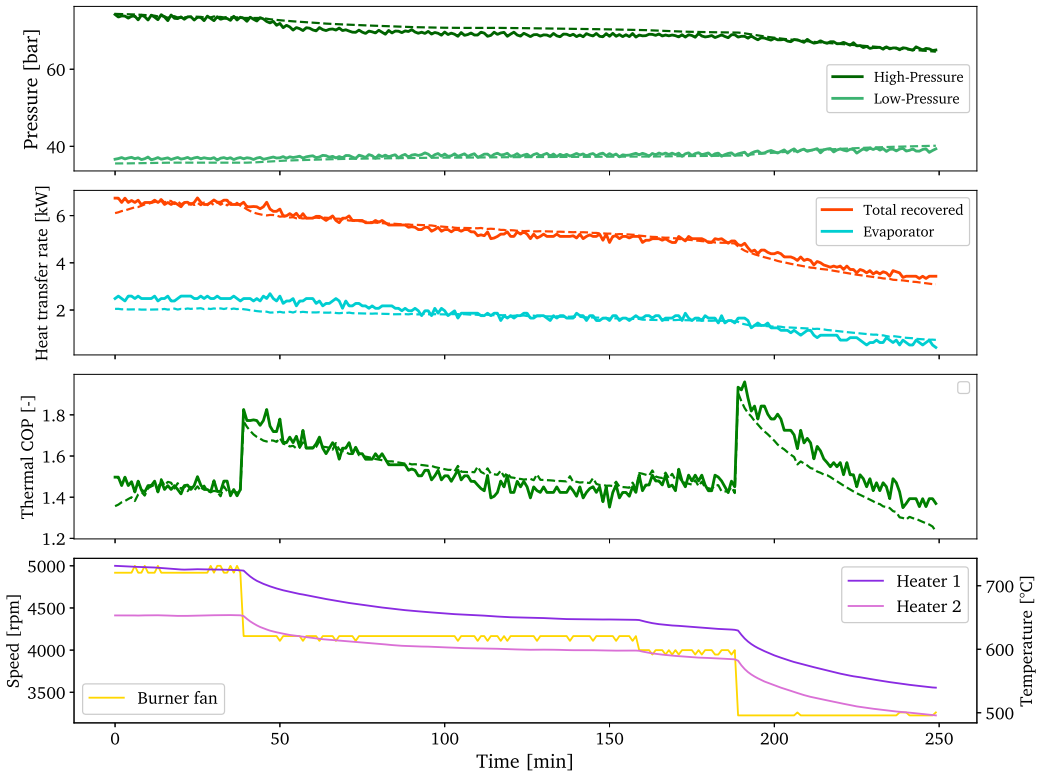


**Figure 18.** TCHP-HYB model transient validation with real experimental data varying the burner fan speed. The real data is in solid, while simulated model is dashed.

**Table 3.** MAPE, MAE (for pressure), and $R^2$ of model output predictions under transient step tests for LPV, HPV, and BF.

| Output | MAPE [%] or MAE [bar] | | | $R^2$ | | |
|---|---|---|---|---|---|---|
| | HPV | LPV | BF | HPV | LPV | BF |
| $p_{ev}$ | 0.97 | 1.2 | 0.68 | −3.1 | 0.93 | 0.65 |
| $\dot{Q}_{ev}$ | 14.4 | 22.2 | 15.2 | 0.40 | 0.72 | 0.81 |
| $p_{gc}$ | 1.5 | 0.84 | 1 | 0.94 | −3.3 | 0.74 |
| $\dot{Q}_{rec,tot}$ | 4.7 | 4.0 | 3.7 | 0.61 | −3.4 | 0.96 |
| $COP_{th}$ | 4.7 | 4.0 | 3.7 | 0.61 | −3.4 | 0.84 |

## 5. Conclusions

This work proposes a general modeling framework for a TCHP application that combines slow and fast dynamics, resulting in the TCHP-HYB model. The approach systematically (i) decomposes the system according to the time scales of its components, (ii) physics-based FV dynamics were assigned to slow states and calibrated quasi-static algebraic relations to fast states, and (iii) couples the submodels through consistent mass and energy balances. While demonstrated on a transcritical $CO_2$ heat pump, the framework is transferable to other vapor-compression and related energy systems. The FV equations (heat exchangers and flash tank) remain unchanged except for thermodynamic property evaluations depending on the chosen refrigerant, while quasi-static correlations (expansion valves and compressors) can be re-identified from new datasets. More specifically, this article discussed the following:

- A brief literature review of dynamic modeling approaches for VCCs in general, and transcritical $CO_2$ cycles in particular, was presented, with emphasis on methods that enable real-time system representation for control design.
- A dynamic model of the TCHP (TCHP-HYB) was developed using the FV method. Slow dynamics (cycle heat exchangers, flash tank, and heater temperature) were represented by differential equations from mass and energy balances on spatially discretized control volumes, whereas fast dynamics (TCs, valves, and the fume heat exchanger) were modeled quasi-statically using empirically tuned correlations.
- The TCHP-HYB model was validated against both steady-state and transient data. Steady-state tests assessed accuracy across operating conditions, and transient tests examined the dynamic response to single-input variations. Acceptable MAPE and $R^2$ in both regimes confirm the model's reliability as a reference for control and optimization studies.

Discrepancies were observed in the influence of LPV variations in high-side pressures and heat rates. This limitation originates from the quasi-static treatment of the mass-flow behaviors of the TCs and expansion valves, which attenuates part of the fast coupling between the low- and high-pressure sides. Future work will incorporate improved dynamic coupling in these components to reduce this gap. Overall, the TCHP-HYB model provides a reliable representation of the real system and illustrates a reusable hybrid modeling strategy for thermodynamic systems with heterogeneous dynamics. Future work will focus on exploiting this model as a foundation for developing reduced-order and control-oriented representations, enabling advanced real-time control strategies such as model predictive control and digital-twin applications.

**Author Contributions:** Conceptualization, A.S.; Methodology, A.S., V.L., P.D. and M.N.; Software, A.S.; Validation, A.S.; Formal analysis, A.S.; Investigation, A.S.; Writing—original draft, A.S.; Writing—review & editing, A.S., V.L., P.D. and M.N.; Supervision, V.L., P.D. and M.N.; Project administration, V.L., P.D. and M.N.; Funding acquisition, V.L., P.D. and M.N. All authors have read and agreed to the published version of the manuscript.

**Funding:** This research was funded by (Association Nationale Recherche Technologie—ANRT): N°2022/0549.

**Data Availability Statement:** The original contributions presented in this study are included in the article. Further inquiries can be directed to the corresponding author.

**Conflicts of Interest:** The authors declare no conflict of interest.

## Abbreviations

**Acronyms**

| | |
|---|---|
| TCHP | Thermal Compressor Heat Pump |
| TC | Thermal Compressor |
| VCC | Vapor Compression Cycle |
| FV | Finite Volume |
| MB | Moving Boundary |
| BUF | Buffer |
| GC | Gas Cooler |
| EV | Evaporator |
| IHX | Internal Heat Exchanger |
| FT | Flash Tank |
| HPV | High-Pressure Valve |
| LPV | Low-Pressure Valve |
| OWV | One-Way Valve |

| | |
|---|---|
| FHX | Fume Heat Exchanger |
| BF | Burner Fan |
| MPG | Monopropylene Glycol |
| LMTD | Logarithmic Mean Temperature Difference |
| $COP_{th}$ | Thermal Coefficient of Performance |
| GPR | Gaussian Process Regression |
| LR | Linear Regression |
| MAE | Mean Absolute Error |
| MAPE | Mean Absolute Percentage Error |
| PRBS | Pseudo-Random Binary Sequence |
| **Symbols** | |
| $T$ | Temperature [K or °C] |
| $p$ | Pressure [bar] |
| $h$ | Specific Enthalpy [$J\,kg^{-1}$] |
| $\rho$ | Density [$kg\,m^{-3}$] |
| $V$ | Volume [$m^3$] |
| $c_p$ | Specific Heat Capacity at Constant Pressure [$J\,kg^{-1}\,K^{-1}$] |
| $U$ | Overall Heat Transfer Coefficient [$W\,m^{-2}\,K^{-1}$] |
| $A$ | Heat Transfer Area [$m^2$] |
| $d_h$ | Hydraulic Diameter [m] |
| $\varphi$ | Valve Opening Ratio [–] |
| $\omega$ | Rotational Speed [rpm] |
| $\dot{m}$ | Mass Flow Rate [$kg\,s^{-1}$ or $g\,s^{-1}$] |
| $\dot{Q}$ | Heat Transfer Rate [W or kW] |
| $R^2$ | Coefficient of Determination [–] |
| **Subscripts and Superscripts** | |
| w | Water |
| mpg | Monopropylene Glycol Loop |
| air | Air |
| fume | Flue Gas/Combustion Exhaust |
| in, out | Inlet and Outlet of a Component |
| sup, ret | Supply and Return Water |
| gc | Gas Cooler |
| ev | Evaporator |
| fhx | Fume Heat Exchanger |
| ihx | Internal Heat Exchanger |
| lpv, hpv, owv | Low-, High-Pressure, and One-Way Valves |
| k1 | Thermal Compressor Cooler Stages 1–3 |
| tc1, tc2, tc3 | Thermal Compressor Stages 1–3 |
| m1, m2, m3 | Motor/Piston Indices (1–3) |
| h1, h2 | Heater Units (1 and 2) |
| $CH_4$ | Methane (fuel) |
| rec, tot | Total Recovered Heat |
| fuel | Fuel Input |
| bf | Burner Fan |
| ref | Reference Condition or Temperature |
| lm | Logarithmic Mean (e.g., $\Delta T_{lm}$) |
| $r_{p1}$, $r_{p2}$, $r_{p3}$ | Pressure Ratio of TC Stages 1–3 |
| th | Thermal (as in $COP_{th}$) |

## References


1. IEA. *World Energy Outlook 2024*; International Energy Agency: Paris, France, 2024. Available online: https://www.iea.org/reports/world-energy-outlook-2024 (accessed on 14 October 2025).
2. Chi, J.; Didion, D. A simulation model of the transient performance of a heat pump. *Int. J. Refrig.* **1982**, *5*, 176–184. [CrossRef]
3. MacArthur, J.W.; Grald, E.W. Unsteady compressible two-phase flow model for predicting cyclic heat pump performance and a comparison with experimental data. *Int. J. Refrig.* **1989**, *12*, 29–41. [CrossRef]
4. Rasmussen, B.P. Dynamic modeling for vapor compression systems—Part I: Literature review. *HVAC&R Res.* **2012**, *18*, 934–955. [CrossRef]
5. Afram, A.; Janabi-Sharifi, F. Review of modeling methods for HVAC systems. *Appl. Therm. Eng.* **2014**, *67*, 507–519. [CrossRef]
6. Eborn, J. On Model Libraries for Thermo-Hydraulic Applications. Ph.D. Thesis, Lund Institute of Technology (LTH), Lund, Sweden, 2001.
7. Bendapudi, S.; Braun, J.E.; Groll, E.A. A dynamic model of a vapor compression liquid chiller. In Proceedings of the International Refrigeration and Air Conditioning Conference, Purdue, West Lafayette, IN, USA, 16–19 July 2002.
8. Quoilin, S. Sustainable Energy Conversion through the Use of Organic Rankine Cycles for Waste Heat Recovery and Solar Applications. Ph.D. Thesis, Université de Liège (ULiège), Liège, Belgium, 2011.
9. Husmann, R.; Aschemann, H. Dynamic modeling of a vapor compression cycle. *IFAC-PapersOnLine* **2022**, *55*, 523–528. [CrossRef]
10. Bendapudi, S.; Braun, J.E.; Groll, E.A. A comparison of moving-boundary and finite-volume formulations for transients in centrifugal chillers. *Int. J. Refrig.* **2008**, *31*, 1437–1452. [CrossRef]
11. Rasmussen, B.P.; Alleyne, A.G. *Dynamic Modeling and Advanced Control of Air Conditioning and Refrigeration Systems*; Technical Report TR-244; University of Illinois at Urbana-Champaign: Urbana, IL, USA, 2006.
12. McKinley, T.L.; Alleyne, A.G. An advanced nonlinear switched heat exchanger model for vapor compression cycles using the moving-boundary method. *Int. J. Refrig.* **2008**, *31*, 1253–1264. [CrossRef]
13. Desideri, A.; Dechesne, B.; Wronski, J.; Van den Broek, M.; Gusev, S.; Lemort, V.; Quoilin, S. Comparison of moving boundary and finite-volume heat exchanger models in the Modelica language. *Energies* **2016**, *9*, 339. [CrossRef]
14. Pfafferott, T.; Schmitz, G. Modelling and transient simulation of $CO_2$-refrigeration systems with Modelica. *Int. J. Refrig.* **2004**, *27*, 42–52. [CrossRef]
15. Rasmussen, B.P.; Alleyne, A.G. Control-oriented modeling of transcritical vapor compression systems. *J. Dyn. Syst. Meas. Control* **2004**, *126*, 54–64. [CrossRef]
16. Zheng, L.; Deng, J.; He, Y.; Jiang, P. Dynamic model of a transcritical $CO_2$ ejector expansion refrigeration system. *Int. J. Refrig.* **2015**, *60*, 247–260. [CrossRef]
17. Ko, J.; Takata, N.; Thu, K.; Miyazaki, T. Dynamic modeling and validation of a carbon dioxide heat pump system. *Evergreen* **2020**, *7*, 172–194. [CrossRef]
18. Diniz, H.A.G.; Paulino, T.F.; Pabon, J.J.G.; Maia, A.A.T.; Oliveira, R.N. Dynamic model of a transcritical $CO_2$ heat pump for residential water heating. *Sustainability* **2021**, *13*, 3464. [CrossRef]
19. Artuso, P.; Tosato, G.; Rossetti, A.; Marinetti, S.; Hafner, A.; Banasiak, K.; Minetto, S. Dynamic modelling and validation of an air-to-water reversible R744 heat pump for high energy demand buildings. *Energies* **2021**, *14*, 8238. [CrossRef]
20. Wolscht, L.; Knobloch, K.; Jacquemoud, E.; Jenny, P. Dynamic simulation and experimental validation of a 35 MW heat pump based on a transcritical $CO_2$ cycle. *Energy* **2024**, *294*, 130897. [CrossRef]
21. Salame, A. *MDPI_paper_codes* (GitHub Repository). Available online: https://github.com/AliSalami98/MDPI_paper_codes (accessed on 14 October 2025).
22. Salame, A.; Lemort, V.; Dufour, P.; Nadri, M. A Dynamic Model for a Multi-Stage $CO_2$ Thermal Compressor Heat Pump Application. In Proceedings of the ECOS 2025, Paris, France, 29 June–4 July 2025. Available online: https://orbi.uliege.be/handle/2268/334624 (accessed on 14 October 2025).
23. Salame, A.; Lemort, V.; Dufour, P.; Nadri, M.; Ibsaine, R. An Empirical Model for a $CO_2$ Thermal Compressor Based on Experimental Data. In Proceedings of the International Compressor Engineering Conference, Purdue University, West Lafayette, IN, USA, 15–18 July 2024; Paper 2868. Available online: https://docs.lib.purdue.edu/icec/2868 (accessed on 14 October 2025).
24. Rossi, T.M.; Braun, J.E. A real-time transient model for air conditioners. In Proceedings of the 20th International Congress of Refrigeration, Sydney, Australia, 19–24 September 1999; Paper 743.
25. Yoon, S.H.; Kim, J.H.; Hwang, Y.W.; Kim, M.S.; Min, K.; Kim, Y. Heat transfer and pressure drop characteristics during the in-tube cooling process of carbon dioxide in the supercritical region. *Int. J. Refrig.* **2003**, *26*, 857–864. [CrossRef]
26. Cheng, L.; Ribatski, G.; Wojtan, L.; Thome, J.R. New flow boiling heat transfer model and flow pattern map for $CO_2$ evaporating inside horizontal tubes. *Int. J. Heat Mass Transf.* **2006**, *49*, 4082–4094. [CrossRef]

27. Shah, M.M. A general correlation for heat transfer during film condensation inside pipes. *Int. J. Heat Mass Transf.* **1979**, *22*, 547–556. [CrossRef]
28. Qiao, H.; Aute, V.; Radermacher, R. Transient modeling of a flash tank vapor injection heat pump system—Part I: Model development. *Int. J. Refrig.* **2015**, *49*, 169–182. [CrossRef]